

On the Reversibility and Fragility of Sodium Metal Electrodes

Yue Deng, Jingxu Zheng, Alexander Warren, Jiefu Yin, Snehashis Choudhury, Prayag Biswal, Duhan Zhang, and Lynden A. Archer*

Metallic sodium is receiving renewed interest as a battery anode material because the metal is earth-abundant, inexpensive, and offers a high specific storage capacity (1166 mAh g^{-1} at -2.71 V vs the standard hydrogen potential). Unlike metallic lithium, the case for Na as the anode in rechargeable batteries has already been demonstrated on a commercial scale in high-temperature Na||S and Na||NiCl₂ secondary batteries, which increases interest. The reversibility of room temperature sodium anodes is investigated in galvanostatic plating/stripping reactions using in situ optical visualization and galvanostatic polarization measurements. It is discovered that electronic disconnection of mossy metallic Na deposits ("orphaning") is a dominant source of anode irreversibility in liquid electrolytes. The disconnection is shown by means of direct visualization studies to be triggered by a root-breakage process during the stripping cycle. As a further step toward electrode designs that are able to accommodate the fragile Na deposits, electrodeposition of Na is demonstrated in nonplanar electrode architectures, which provide continuous and morphology agnostic access to the metal at all stages of electrochemical cycling. On this basis, nonplanar Na electrodes are reported, which exhibit exceptionally high levels of reversibility (Coulombic efficiency >99.6% for 1 mAh cm^{-2} Na throughput) in room-temperature, liquid electrolytes.

1. Introduction

It can be said that rechargeable batteries have played a fundamental role in enabling the age of information, for only their

small sizes and excellent ability to reversibly convert and store electrical energy made portable electronic devices possible. Rechargeable lithium-ion batteries (LIBs) in which a graphitic carbon material hosts lithium in ionic form as LiC₆ and in which transition metal oxides are used as cathode (e.g., LiCoO₂, Li_{1.2}Ni_{0.15}Co_{0.1}Mn_{0.55}O₂, etc.) currently dominate the marketplace. LIBs are well positioned to continue this dominance as demands grow for energy dense storage in areas ranging from transportation to grid storage, and ultimately to autonomous/untethered robotics. Unfortunately, the specific energy output from LIBs though close to the maximum theoretical limit for this chemistry is unsatisfyingly low and battery costs remain high, in spite of developments in manufacturing processes and electrode formulations that replace expensive Co with Ni in the cathode. At current trends, it is also difficult to see how battery system acquisition costs for LIB technology will achieve the <\$50 per kWh and >2000 cycles of trouble-

free operation required to achieve amortized costs compatible with the falling leveled costs (\$0.08 per kWh–\$0.03 per kWh) of electricity generated from solar or wind.^[1]


A rechargeable battery technology, which replaced the graphitic carbon host material at the anode with an electrochemically active metal such as Li or sodium (Na) could produce substantial increases in storage capacity of the battery anode (from 360 to 1166 mAh g^{-1} (for Na) or 3860 mAh g^{-1} (for Li)), lowering anode material costs.^[2] Such rechargeable metal anode batteries would also enable use of commensurate high-energy cathode materials, such as sulfur (S₈)^[3–5] and oxygen/carbon dioxide (O₂/CO₂) mixtures,^[6–13] among others. Use of rechargeable batteries in which an energy-dense metallic anode is paired with an energy-dense cathode offer potential for significant improvements in specific energy on either a volumetric or mass basis (e.g., $SE_{\text{Li-ion}} = 0.15 \text{ kWh kg}^{-1}$ or 0.25 kWh L^{-1} ; $SE_{\text{Li-S}} = 2.5 \text{ kWh kg}^{-1}$ or 2.8 kWh L^{-1} ; $SE_{\text{Li-O}_2/\text{CO}_2} = 10.5 \text{ kWh kg}^{-1}$; $SE_{\text{Na-S}} = 1.25 \text{ kWh kg}^{-1}$ or 1.5 kWh L^{-1} ; $SE_{\text{Na-O}_2/\text{CO}_2} = 4 \text{ kWh kg}^{-1}$). Even after accounting for the typical factor of 3–4 reduction in practical storage capacity due to the weight of the inactive components in any battery (e.g., packaging, electrolyte, current collectors, separator, conductivity additives, cell controls), any of these battery chemistries would produce improvements in specific energy relative to today's LIB technology.

Y. Deng, J. Zheng
Department of Materials Science and Engineering
Cornell University
Ithaca, NY 14853, USA

A. Warren, Dr. S. Choudhury, P. Biswal, Prof. L. A. Archer
Robert Frederick Smith School of Chemical
and Biomolecular Engineering
Cornell University
Ithaca, NY 14853, USA
E-mail: laa25@cornell.edu

Dr. J. Yin
Cornell Energy Systems Institute
Cornell University
Ithaca, NY 14853, USA

D. Zhang
Department of Mechanical Engineering
Cornell University
Ithaca, NY 14853, USA

 The ORCID identification number(s) for the author(s) of this article can be found under <https://doi.org/10.1002/aenm.201901651>.

DOI: 10.1002/aenm.201901651

Rechargeable batteries based on sodium anodes are of specific interest in the present study for at least three reasons. First, technical barriers—uncontrollable loss of active Na due to parasitic reactions between the reactive anode and components in typically used liquid electrolytes;^[14] nonuniform, dendritic electrodeposition, and dendrite-induced fast electrolyte consumption makes it challenging for Na metal cells to reach long cycle life.^[15–17] Meaning that development of fundamentally based strategies that enable development of Na anodes with high reversibility would provide clues about how to address similar technical barriers that have limited progress toward secondary batteries based on less reactive alkali metals, including Li and K as anodes. Second, high-temperature rechargeable batteries based on Na anodes have already been demonstrated at commercial scale in multiple cathode chemistries.^[18,19] Finally, a successful rechargeable battery platform, in which an intrinsically low-cost cathode material, e.g., elemental sulfur, is paired with an earth-abundant and low-cost Na anode would open opportunities for creating cost-effective, but high-performance electrical energy storage solutions to address cost barriers in sectors of commerce (e.g., grid storage), where low cost storage is a requirement for achieving fossil-fuel scale dispatchability of electric power generated from renewable sources.

In situ optical visualization has been applied in previous studies to interrogate morphological evolution at Na electrodes.^[17,20] By performing these measurements at more realistic current densities and in O-ring cells that make it possible to separate the effects of mechanical pressure imposed by a separator on the evolution of Na electrodeposition morphology, the present study enables a more in-depth analysis of failure modes and reversibility of the Na metal electrode. A key finding is that while morphological and chemical instability of Na lead to very low-efficiency and nonplanar/mossy deposition during battery recharge, orphaning (electrical disconnection and physical loss of Na) during anode discharge is by far the most important determinant of anode reversibility. Specifically, we observe that the low Coulombic efficiency (CE) of Na electrodes results primarily from mechanical breakage and subsequent electronic disconnection of large fragments of low-density, mossy Na electrodeposits from the electrode mass. We find further that by constraining the deposition in a generic structured electrode architecture composed of interwoven carbon fibers and with average pore sizes ($\approx 10\ \mu\text{m}$) that are a fraction of the mossy deposit dimension ($\approx 400\ \mu\text{m}$ in the case of free Na electrodeposition growth, and $50\ \mu\text{m}$ in the case where the Na deposit growth is constrained by the woven carbon fabric), it is possible to utilize nearly the full Na electrode mass, even without the need to apply mechanical pressure to the electrode via a separator. On this basis, we report that it is possible to achieve Na anodes with unprecedented, high CE values, exceeding 99% in many cases in liquid electrolytes. Our results confirm that orphaning of Na plays a key role in its notoriously poor reversibility. Finally, we show that rechargeable batteries that pair a highly reversible Na anode with a sulfur/carbon composite (MCPS) cathode reported in our earlier work,^[4,5] exhibit impressive overall reversibility and cycling behaviors.

2. Results and Discussion

2.1. Optical Visualization of Na Deposition on Planar Substrates

The apparatus shown in **Figure 1** was used to track the time-dependent nucleation and growth of Na electrodeposits on a planar electrode substrate. The visualization cell is compatible with various thin electrode substrates, including copper (Cu) foil and stainless steel (SS) plates, but in this paper all visualization experiments were performed using Na as the substrate. The apparatus consists of a custom-designed two-electrode electrochemical cell that is small enough to fit inside a sealed quartz cuvette composed of planar windows on all sides. The cuvette is designed to fit in the sample compartment of an Olympus upright optical microscope outfitted with extra-long working distance objectives and video recording equipment capable of grabbing images at a rate of 300 frames per second. All experiments reported in the present study used an electrolyte composed of $1\ \text{M}\ \text{NaClO}_4$ and a carbonate solvent mixture that was prepared by mixing equal volumes of ethylene carbonate (EC) and propylene carbonate (PC). Measurements were performed in a configuration where the light path and imposed electric field were approximately orthogonal. The cell is interfaced with a potentiostat, which allows simultaneous application of a fixed current and measurement of the overall voltage response as Na is stripped from one electrode and plated onto the next. By performing measurements, in which the electrode polarity is periodically switched, it is possible to directly visualize changes in Na electrodeposition morphology over multiple cycles of plating and stripping from a planar electrode.

Figure 2a–f are snap-shots of videos collected at different time points in the optical cell during galvanostatic sodium plating and stripping processes, respectively, at a fixed current density of $2\ \text{mA}\ \text{cm}^{-2}$. **Figure 2g** is the corresponding voltage profile, which demarcates the voltages, at which images reported as **Figure 2a–f** were collected. **Figure 2a** taken at $t = 0$ of the second discharge/stripping cycle, for example, shows that well-formed mossy deposits are formed at the electrode surface after the previous charge/plating cycle. As the discharging progresses, the Na deposits are observed to first slowly decrease in size (see **Figure 2b**) and shortly thereafter appear to cease changing in size (**Figure 2c**). Continuation of the discharge process leads to a regime where the largest structures appear to become physically elongated in the field direction and to shrink in the lateral direction (**Figure 2d**). Shortly thereafter the deposits appear to completely de-bond from the substrate, such that by the end of the discharge (**Figure 2e**) none of the initial deposits can be seen on the electrode surface.

We quantify changes in the dimensions of a typical large Na deposit normal and parallel to the electrode surface in **Figure 2h** during once cycle of charge and discharge. It is seen that the Na deposits grow more quickly in the lateral dimension than in the direction normal to the electrode surface. **Figure 2h** reveals further that during the charge process, the deposits initially grow in both dimensions, but ultimately reach a plateau where growth is uniformly slow. Additionally, during the discharge the deposit shrink primarily in the lateral direction and at a certain point (13 min of the experiment) the deposits begin to shrink rapidly in the lateral direction and after a brief period

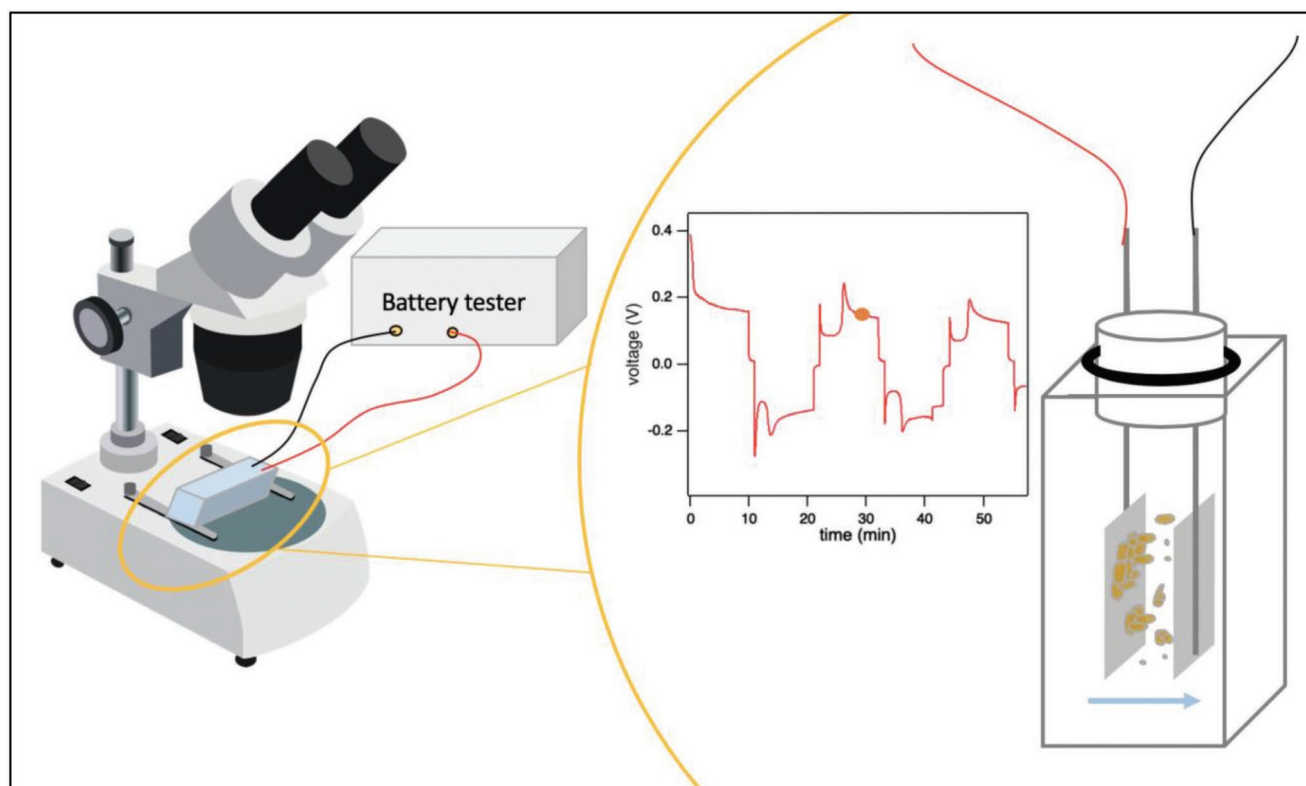


Figure 1. Schematic drawing of the visualization experiment setup. The orange dot on the voltage profile reflects the point that corresponds to the stage of deposition of Na ions in the visualization cell illustrated to its right. The blue arrow indicates the direction in which Na^+ ions migrate.

of stretching (see Figure 2d) in the vertical direction, rapidly break away from the electrode surface and disappear from the field of view. This sequence suggests that the stretching of the mossy deposits is produced by weakening of the connections to the underlying Na. Physical breakage and mechanical removal of the rough Na deposits, as opposed to electrochemical reversibility of the underlying electrodeposition reaction, therefore seems a more plausible source of both the rapid electrodeposition disappearance observed in Figure 2e and the sudden drop observed after the 13 min timepoint in Figure 2h. These results underscore the importance of the direct visualization experiments. Specifically, without information about the sequence of events that preceded the apparent complete removal of Na electrodeposits observed in Figure 2e, one might have erroneously concluded, from before and after type electron microscopy analysis of the electrode surface that electrodeposition reactions at the Na electrodes are highly reversible.

Analysis of the voltage profile in Figure 2g provides additional insights about the discharge reaction at the Na electrode. The dual peaked shape of the time-dependent discharge voltage can be compared to the analogous profiles reported during discharge/stripping of Li electrodeposits. The peaks have been traditionally associated with the large resistances that must be overcome in first stripping Li from under the SEI formed on the fresh deposits and secondly in stripping Na from under the better developed SEI at the planar electrode/electrolyte interface, in a process termed pitting.^[21] A difference with the voltage profile for Na, however, is that whereas Li manifests a

single plateau regime (Figure 2b) associated with the ease of stripping Li once the first SEI layer is breached, the voltage profile for Na manifests two plateau regimes (Figure 2b,d). By analogy to the Li case, we attribute the first voltage plateau to the ease of stripping Na from the mossy deposits—i.e., once the SEI is breached.

The source of the second plateau in Figure 2d is presently unknown but can be reasonably well attributed to an advanced form of the pitting process, where it possibly results in more extensive removal of Na from under the SEI formed on the original planar Na electrode (i.e., from under the mossy Na electrodeposition). This interpretation is supported by the apparent stretching of the largest deposits in step Figure 2d and removal of nearly all mossy Na deposits from the electrode in step Figure 2e. Specifically, we attribute the stretching of the mossy Na electrodeposits to weakening of their connections to the underlying/bulk Na electrode and their ultimate removal to breakage of these connections, resulting in physical disconnection of the mossy structures from the electrode. This sequence of events is also consistent with direct observations (see Video S1 in the Supporting Information), where the disconnected, low-density mossy electrodeposits are seen to quickly drift to the surface of the electrolyte. We note further that consistent with the periodicity is observed in the voltage profile (Figure 2g), the same sequence of events occur over every discharge cycle (e.g., see Figure 2f), which quickly fills up the electrolyte with disconnected fragments of mossy (orphaned) sodium, ultimately shorting the cell.

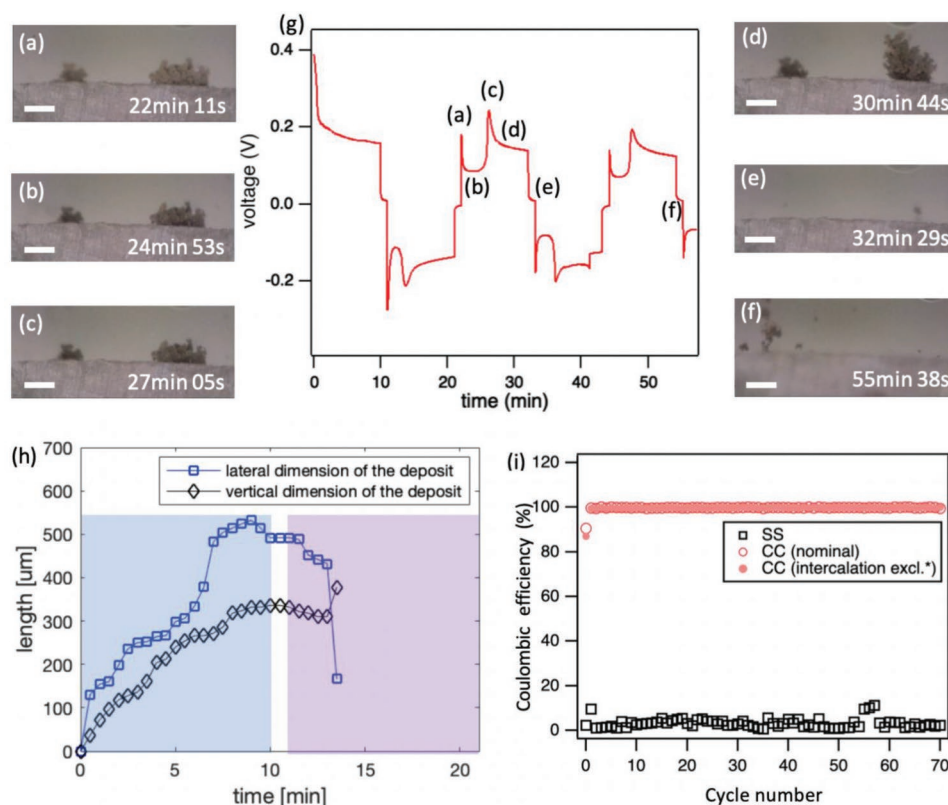


Figure 2. Visualization results reflecting the physical losing of Na during plating-stripping cycles. a–f) Still frames from video (Video S1, Supporting Information) showing how the anode surface was cleaned after a stripping cycle. Scale bar 400 μm. g) Corresponding voltage profile for the in situ optical observation of stripping and plating. h) How the size of a single mossy Na deposit varies with time in a complete charging-discharging cycle (Video S2, Supporting Information). The mossy deposit described here is neither one shown in (a–f). $t = 0$ is set to be the beginning of the charging cycle, not the real time. Blue shaded region corresponds to the charging cycle, where purple shaded region corresponds to the discharging cycle. White region corresponds to the resting period. $J = 2 \text{ mA cm}^{-2}$. i) CE cycling result of various counter electrodes with 1 mAh cm^{-2} Na throughput and a rate of $J = 0.5 \text{ mA cm}^{-2}$. “SS” stands for stainless steel, and “CC” stands for carbon cloth. *The method used to estimate the intercalation capacity is described in the Supporting Information.

The accumulation of orphaned Na apparent from the optical visualization experiments is indicative of an extremely low reversibility of the Na metal electrode under the measurement conditions. We quantified the reversibility of the Na electrodes in a Na||stainless steel coin cell by measuring the Coulombic efficiency under galvanostatic cycling at 0.5 mA cm^{-2} . To replicate conditions in the visualization cell, the electrodes were separated by a Teflon washer (O-ring)/spacer, which allows us to eliminate the effect of mechanical pressure on electrode reversibility. The CE was determined by first plating a fixed capacity (1 mAh cm^{-2}) of Na onto the stainless steel electrode during the charge cycle and subsequently measuring the capacity of Na recovered when the stainless steel electrode is fully discharged. As shown in Figure 2i, the average CE is extremely low (CE $\approx 2.98\%$), confirming the poor reversibility of the Na electrode. The extremely low CE values also are consistent with the hypothesis that the rapid Na orphaning observed in the visualization experiments leads to poor access to the full electrode capacity during subsequent cycles. It is then not difficult to imagine the situation apparent in Figure 3b,c, in which large amounts of orphaned Na quickly accumulate in the inter-electrode space. As a final assessment of our hypothesis we replaced one of the Na electrodes with a carbon fiber fabric

that in principle facilitates electrical access to the orphaned Na. The results shown in Figure 2i clearly demonstrate the effectiveness of the concept in improving electrode reversibility; we discuss its practical utility for reversible Na electrode design in Section 2.3.

Figure 3b,c are snapshots taken from visualization cells at discrete time points during galvanostatic cycling at 4 mA cm^{-2} . It illustrates the large amounts of orphaned Na that is generated in each cycle. It is remarkable, nonetheless, to see that the corresponding voltage profile (Figure 3a) shows no obvious signs of accumulation of the electronically inaccessible fragments of the Na electrode in the cell. We attribute this observation to the fact that the orphaned Na is both soft and porous. The softness allows the material to accumulate in the inter-electrode space before creating a percolated electronic conduction pathway that would short-circuit the cell. The porous structure would minimize the effect of orphaned Na on the ion-transport rates in the electrolyte.

To understand the role of a separator in limiting orphaning and for promoting reversibility of a Na anode, we created conventional symmetric Na||Na coin cells using glass fiber as the separator and analyzed their performance in galvanostatic strip/plate cycling measurements. A typical voltage profile obtained

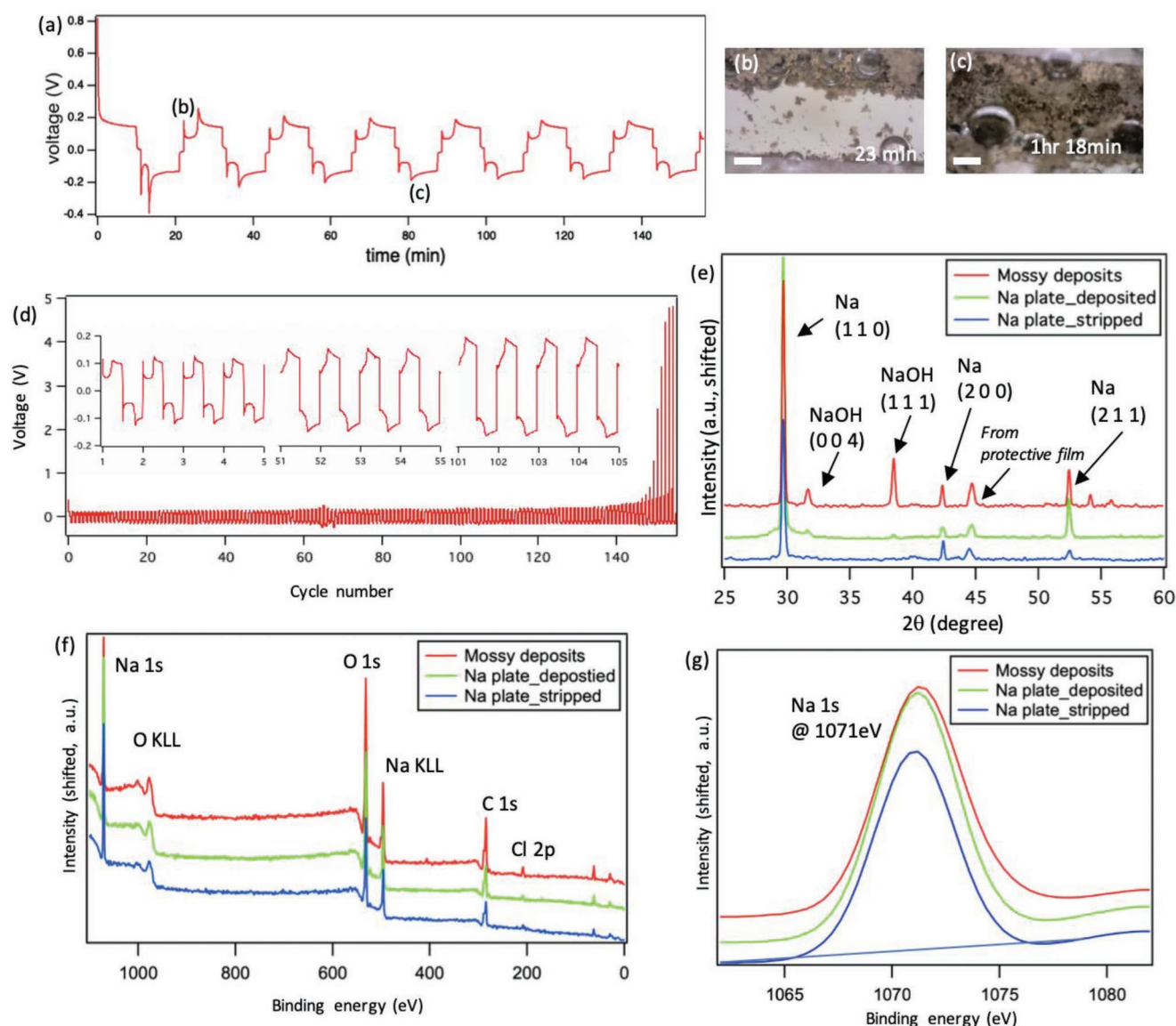


Figure 3. Characterization of Na deposits on their electrochemical and chemical properties. a) Corresponding voltage profile for an in situ optical observation of plating and stripping, $J = 4 \text{ mA cm}^{-2}$. b, c) Still frames from video revealing the amount of orphan Na created during cycling. Scale bar 400 μm. d) Plating-stripping voltage profile for a Na–Na symmetric coin cell, $J = 0.5 \text{ mA cm}^{-2}$. e) XRD results of mossy deposits preserved in the glass fiber separator (red), pristine Na metal electrode that was constantly deposited with Na at $J = 0.5 \text{ mA cm}^{-2}$ (blue), and pristine Na metal electrode that was constantly deposited with Na at $J = 0.5 \text{ mA cm}^{-2}$ (black). f) XPS data of three samples that represent various form of sodium. g) Zoomed-in Na 1s peak from (e).

at a current density of 0.5 mA cm^{-2} is provided in Figure 3d. The initial cycles show the same distinct double-plateau characteristic profile observed for the visualization cell, which indicates that even with a separator in place, the orphaning process develops in a similar manner. At later cycles, the profiles are seen to change shape and the two distinctive plateaus associated with steady Na-plating and pitting, respectively gradually disappear and the peak-to-peak cell voltage rises. Based on visualization results in Figure 3b,c, we attribute these changes respectively to the thickening of the SEI on the Na deposits over time; the steady increase in the etching depth into bulk Na needed to compensate for the large amount of orphaned Na that accumulates in the cell; and the eventual clogging of the

ion transport pathways produced by orphaned Na in the more limited space available in the separator.

2.2. Chemical Analysis of Na Electrodeposits

To determine the chemical composition of the orphaned Na, X-ray diffraction (XRD) and X-ray photoelectron spectroscopy (XPS) were used to analyze the composition of the mossy, but connected, Na structures present on the surface of the bulk Na electrode as well as the mossy, orphaned Na harvested from the electrolyte/separator of symmetric Na cells after cycling. Glass fiber separators were found to be particularly useful for

harvesting the orphaned Na deposits (see Figure S2a–c, Supporting Information), for more in-depth chemical analysis. The results from XRD and XPS analysis are reported in Figure 3e–g and compared with the analogous information for a pristine Na metal electrode exposed to the same electrolyte and discharged for an hour to account for the effects on composition changes induced by the electrolyte. The XRD results (Figure 3e) show that the mossy Na deposits are essentially Na metal with a body center cubic (bcc) lattice structure, which has nearly the same lattice constant as the bulk sodium.

To minimize sample degradation from atmospheric exposure of Na, XPS measurements used a specially designed puck that allows samples to be directly transferred from a glovebox to the XPS instrument for analysis. Results reported in Figure 3f,g show that both the Na 1s and Na KLL peaks present on the surface of the pristine Na electrode are also present on the mossy deposits either harvested from the separator or present on the Na electrode after cycling. It is also significant that no binding energy shifts are seen for either the Na 1s or Na KLL, which suggests that irrespective of the source, the Na atoms in the mossy structures have the same orbital configurations as those in the bulk Na metal. These results therefore lead us to conclude that the chemistry of the orphaned Na is principally the same as bulk Na.

2.3. Electrode Architectures for Limiting Na Orphaning

Learning that the orphaned Na structures have similar surface chemical features as bulk Na metal exposed to the same electrolyte, we studied the effect of the Na electrode design on reversibility. As previously shown in Figure 2i, the CE of a Na||stainless steel cell using a Teflon washer (O-ring) to hold the electrolyte is $\approx 3\%$. As a first test of our hypothesis that this low CE results primarily from electrical disconnection and orphaning of the large amounts of mossy Na deposits observed to fill the inter-electrode space in our visualization experiments, we considered the effect of pressure imposed by a separator in limiting Na orphaning. A glass fiber separator was added between the Na and stainless steel electrode in the same O ring cell. As shown in Figure 4a, this change caused the CE to increase from 3% to 39% but produces no significant difference in the reversibility of Na—either when SS or Cu are used as the counter-electrode. The higher CE values measured in cells that used a glass fiber separator are close to the previously reported value of $\approx 20\%$.^[14] Our results therefore imply that while pressure induced by a separator can be effective in limiting Na orphaning, it cannot completely stop it (as evidenced by the large amounts of mossy Na trapped in the glass fiber separator (Figure 3e) and by the poor reversibility of the Na anode apparent in Figure 4e).

The ease with which the orphaned Na is trapped in a glass fiber separator suggests that an electrode architecture with a similar porous, net-like structure, but in which the structures forming the net are electronically connected up to the macroscale would be an effective strategy for both capturing the orphaned Na and for maintaining its electrochemical activity in a battery.^[21] With guaranteed electronic access to prevent physical loss, we hypothesize that such an electrode architecture could dramatically improve reversibility of a Na electrode.

To evaluate the concept, we used a commercial conductive cloth composed of woven conductive carbon fibers as the current collector in our original O-ring cells, which do not use a separator. Results reported in Figure 2i show that CE values exceeding 99.6% and high levels of reversibility are achieved without the need for a separator and without any efforts to optimize the electrolyte to reduce chemical instability of the Na electrode. Addition of a glass fiber separator to these cells (see Figure 4a) produce only a small additional improvement. The electrode architecture therefore plays a dominant role in improving the reversibility of the Na electrode.

We note that in addition to serving as a substrate for Na deposition, a CC electrode can also host Na^+ ions intercalated between the graphitic carbon layers. Traditionally graphitic carbons are considered poor hosts for Na^+ ions^[22,23] due to both the unstable nature of Na-graphite intercalation compounds^[24] and the co-intercalation of solvents^[25] (such as the carbonates used in this study). Results reported in Figure S3 (Supporting Information) show that the interplane carbon spacing of the CC electrodes exposed to the PC based electrolytes is larger than regular graphite and there is evidence (Figure S4, Supporting Information) that contrary to conventional thinking, the CC electrodes can reversibly store a small capacity ($\approx 0.2 \text{ mAh cm}^{-2}$) of Na^+ at low current densities. The CE values reported in Figure 4a, are corrected values for which the capacity produced by Na^+ intercalation (see Figure S4 in the Supporting Information) has been removed.

To evaluate the hypothesis that the carbon fiber cloth enhanced reversibility of the Na anode by preventing electrical disconnection of Na, we analyzed the Na deposits on the electrode in the fully charged and fully discharged states using X-ray powder diffraction. The result is presented in Figure 4b and shows that for the fully charged electrode the typical Na diffraction peaks are absent, but two prominent peaks uniquely identified as the (0 0 4) and (1 1 1) peaks of orthorhombic sodium hydroxide (NaOH) are observed. Upon discharging the electrode, both peaks are seen to completely disappear. These results are consistent with our hypothesis but require an assumption that the NaOH peaks are surrogates for Na that has reacted with environmental moisture and air during the sample transfer to the XRD. This assertion is evaluated using scanning electron microscope (SEM) imaging with energy-dispersive X-ray (EDX) mapping of the charged and discharged electrodes. An advantage of the SEM analysis is that the sample exposure to atmospheric moisture is avoided. For the fully charged electrode Figure 4c–e shows a smooth, even, and dense deposit of Na that covers each of the carbon fibers. We attribute this observation to both the good wetting of the CC electrode by the electrolyte and to the lower effective deposition current density at the higher surface area carbon fibers. Figure 4f–h shows the analogous result when the electrode is fully discharged. It is seen that the Na coating completely disappears, confirming the source of the high reversibility of the carbon fiber cloth electrode. Figure S2d–f (Supporting Information) further shows that excess Na tends to deposit inside rather than on the surface of the CC.

To further evaluate the benefits of a woven carbon framework for hosting Na deposition, we created a Na-carbon cloth (CC) anode by first electrochemically depositing Na to CC in

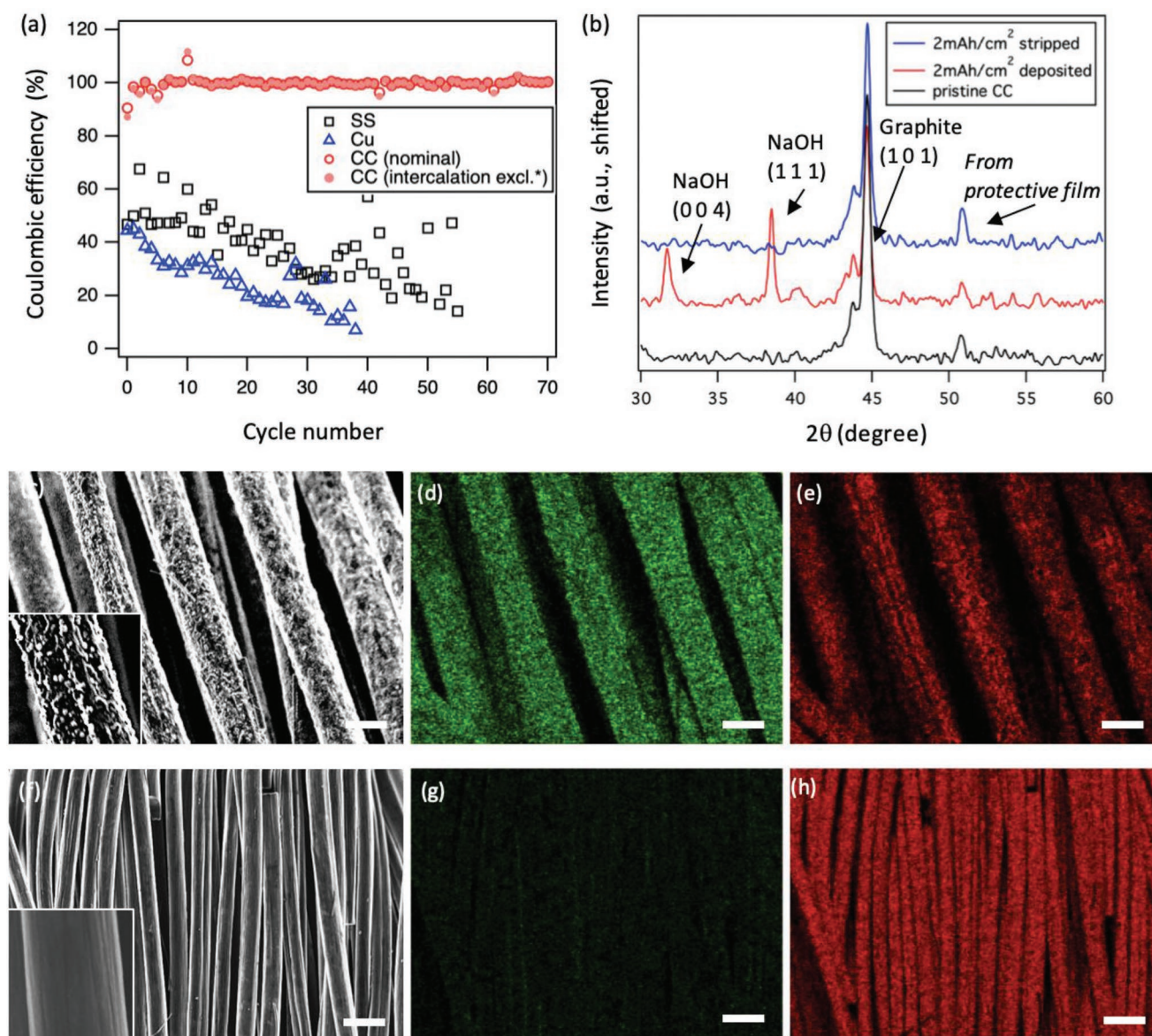


Figure 4. Reversibility of Na deposits on various substrates. a) CE cycling result of various counter electrodes with 1 mAh cm⁻² Na throughput and a rate of $j = 0.5$ mA cm⁻². “SS” stands for stainless steel, “CC” stands for carbon cloth, and “Cu” stands for copper. Separator used for this test was glass fiber. *The method used to estimate the intercalation capacity is described in the Supporting Information. b) XRD results showing the reversibility of Na deposits on CC. c) SEM image of a carbon cloth loaded with a 2 mAh cm⁻² Na throughput and a rate of $j = 1$ mA cm⁻². Scale bar 10 μm. d, e) EDX mappings for sample shown in (c), where (d) is the Na mapping and (e) is the C mapping. Scale bar 10 μm. f) SEM image of a stripped carbon cloth with a previous Na throughput of 2 mAh cm⁻² and a discharge rate of $j = 1$ mA cm⁻². Scale bar 25 μm. g, h) EDX mappings for sample shown in (f), where (g) is the Na mapping and (h) is the C mapping. Scale bar 25 μm. Brightness of all EDX maps has been normalized.

a Na||CC cell. The resultant Na-infused CC electrode was used as the anode in an electrochemical cell in which it was paired with a carbon-sulfur composite cathode prepared according to the procedure reported by Wei et al.^[4] The results reported in **Figure 5a** compare the discharge properties and Columbic Efficiency of Na-Cu||S and Na-CC||S cells in which anodes composed of 3 mAh cm⁻² (or roughly 2.57 mg cm⁻²) of Na deposited on either a planar Cu or nonplanar CC electrode were paired with a sulfur-carbon composite cathode. The active material loading in the sulfur cathode is 1.39 mg cm⁻², which yields a theoretical capacity of 2.4 mAh cm⁻² and a low theoretical N/P

ratio (N/P = 1.25) for the cells. Results from initial galvanostatic cycling experiments nonetheless show that at a current density of 0.5 mA cm⁻² only a fraction of sulfur’s theoretical capacity (0.43 mAh cm⁻²) is maintained. Based on this observation and the high efficiency cycling already demonstrated for the Na-CC anode, the real N/P ratio for the Na-CC Na-CC||S cells is ≈7. The figure also presents results for Na||S cells in which a Na sheet with capacity of ≈40 mAh cm⁻² is paired with the same sulfur-carbon composite cathode for an equivalent N/P ratio of 93. The results show that while the Na-Cu||S loses its initial capacity within the first 20 cycles, the Na||S cells with a

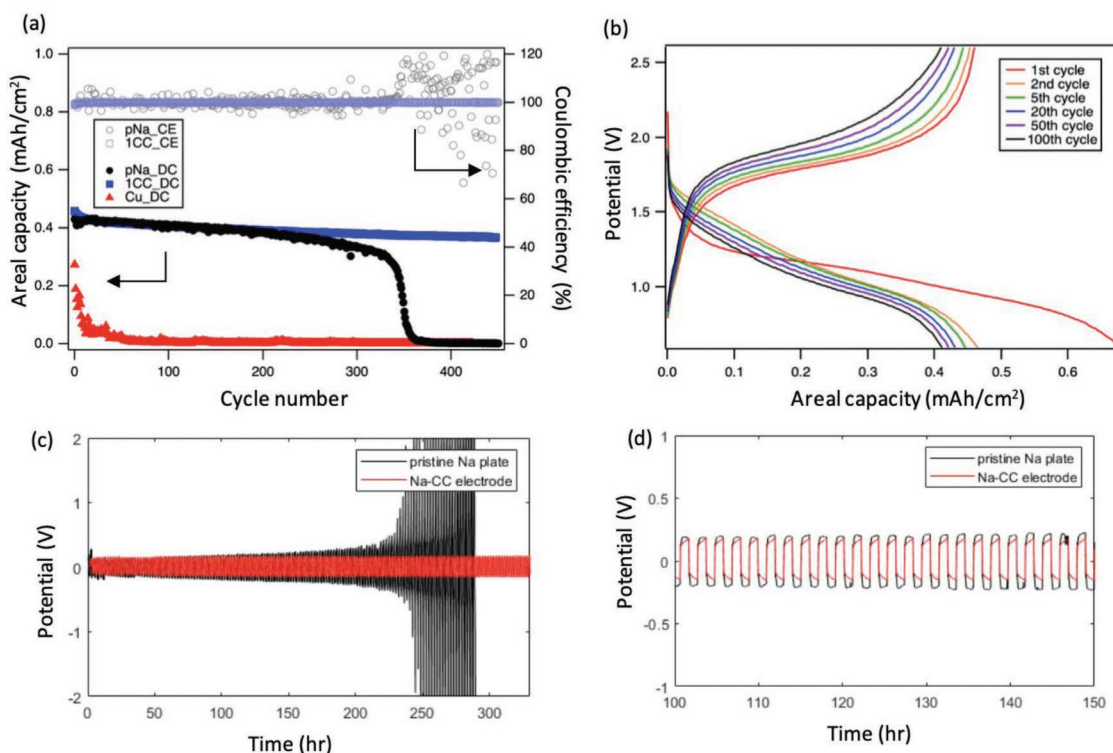


Figure 5. Apply Na-CC anodes in electrochemical cells. a) Coulombic efficiency (CE) and discharge capacity (DC) for a room temperature Na||S full-cells cycled at a fixed rate of 0.2 C. The notation “pNa” stands for pristine Na metal plate; “Cu” for planar copper electrode. We note that large fluctuations in the CE values for the planar control analog of these cells in which Cu foil is used as a current collector prevent us from including these results in the figure; they are instead reported in Figure S8 (Supporting Information). The loading of Na-CC and Na-Cu anodes are both 3 mA h cm⁻², which gives an N/P ratio of roughly 7. b) Capacity–voltage plot for a room-temperature Na-CC||S cell at a fixed rate of 0.2 C. c) Stripping and plating results for symmetric Na cells with pristine Na metal electrodes and Na-CC electrodes on both sides, respectively. $J = 0.5 \text{ mA cm}^{-2}$, and each charging/discharging half cycle is an hour. d) 100–150 h plot for (c).

greater N/P ratio exhibit stable cycling for at least 350 cycles. Remarkably the Na-CC||S cells with the same N/P ratio for the Na–Cu||S cells retain greater than 80% of their initial capacity at the 450th cycle. Figure 5b shows further that the charging and discharging profiles for the Na-CC||S preserve their shape over at least 100 charge/discharge cycles, supporting the argument that the Na-CC anode is a promising electrode architecture for achieving high levels of reversibility in a Na metal anode. Figure 5c,d presents the electrochemical performance of the Na-CC hybrid anode in a stripping and plating test. The control cell, with loading of 1165 mA h g⁻¹ (or roughly 40 mA h cm⁻²) and therefore much more Na available, failed at the around 230th cycle. However, the Na-CC symmetric cell with only 300 mA h g⁻¹ loading (or 3 mA h cm⁻²) on each side, is stable for >350 cycles, which further proves the accessibility of Na deposited in the CC matrix. The peak-to-peak potentials for both cells were similar, implying that Na in the Na-CC anode behave similarly as bulk Na.

3. Conclusions

In this study, we investigate the reversibility of sodium metal electrodes in liquid electrolytes using optical visualization studies in symmetric cells. We report that sodium deposits as

low mass density structures over a wide range of current densities. The extremely soft and fragile nature of the mossy Na deposits lead to failure by an orphaning process, wherein Na structures deposited in a previous cycle, physically break away from the current collector during the subsequent stripping cycle to become electronically disconnected from the Na electrode mass, quickly filling the inter-electrode space with metal fragments. Chemical and X-ray analysis of the fragments confirm that they are essentially Na metal, indicating that the orphaning process is not a result of detrimental reactions between the Na electrode and electrolyte components.

Unlike Li metal batteries, which have been reported to fail when mossy/dendritic deposits penetrate the separator and internally short-circuit the cell, here we find that Na metal cells typically fail due to the physical loss of the active anode material and consumption of electrolyte needed to recreate the solid-electrolyte interphase on the anode. We explore the use of nonplanar electrode architectures, which are designed to provide morphology agnostic frameworks for maintaining electronic access to Na deposits. It is reported that in a 1 M NaClO₄-EC/PC liquid electrolyte and for a 1 mA h cm⁻² Na throughput, a hybrid Na/carbon cloth (CC) anode exhibits dramatically higher Coulombic Efficiency (>99.6%), in comparison to a conventional planar Na anode (CE ≈ 38.6%) in the same electrolyte. It is shown further that the anode

architecture is primarily responsible for its high levels of reversibility and that room-temperature Na-S cells that pair the hybrid Na-CC anodes with sulfur-carbon composite cathodes exhibit stable cycling.

4. Experimental Section

Materials: Electrolyte used in this study was NaClO₄ in EC/PC solution (50:50 by volume), prepared in the laboratory. All materials were kept under argon gas, and the electrolyte was extra dried with molecular sieve for overnight before using. Na metal used was purchased from Sigma Aldrich (cubes, under mineral oil, 99.9% trace metals basis).

Visualization: Visualization cells were quartz 3.5 mL cuvette purchased from Science Outlet (schematic shown in Figure 1), with paired caps made in the laboratory. Optical microscope used in this study were OLYMPUS DP 80 and Dino-Lite, and the battery tester used was Neware CT-3008W coin cell testing system. Electrolyte and Na plates used were as described in the “Materials” Section. Measurements were carried under room temperature and pressure.

Coin Cell Electrochemical Tests: Two types of coin cells were assembled in this study. One used Teflon washer as the separator, with thickness about 0.8 mm and a hole in the center with diameter of 3/8”. The other type used glass fiber GF/D, purchased from Sigma Aldrich. Glass fiber plates were kept in 100 °C oven overnight for water removal. Electrolyte and Na plates used were as described in the “Materials” Section. Plain carbon cloth 1071 HCB (from Fuel Cell Store) was first washed in acetone and dried in 100 °C oven overnight before using for the CC counter electrode and CC/Na anodes. All tests were performed on the Neware CT-3008W coin cell testing system. Measurements were carried under room temperature and pressure.

Characterization: SEM and EDX images were taken on a Zeiss GEMINI 500 Scanning Electron Microscope. XPS data was collected by technician at Cornell Center for Materials Research Shared Facilities, while samples were carried to the facility in an air-tight chamber filled with argon gas. Sample transfer to the instrument was done under nitrogen before it was loaded into the vacuum chamber. XRD data was collected from a Bruker D8 Advance ECO powder diffractometer, with Cu K α source. Parafilm was used to protect the samples from being oxidized, while samples were previously dried under vacuum. Raman spectra were collected via a Renishaw InVia Confocal Raman microscope, with all the samples open to the air.

Supporting Information

Supporting Information is available from the Wiley Online Library or from the author.

Acknowledgements

The research was supported as part of the Center for Mesoscale Transport Properties, an Energy Frontier Research Center supported by the U.S. Department of Energy (DOE), Office of Science, Basic Energy Sciences, under Award DE-SC0012673. The work made use of the Cornell Center for Materials Research Shared Facilities, which are supported through the NSF MRSEC program (DMR-1719875). The authors are very grateful to Dr. Shuya Wei, Dr. Yusuke Hibi, Dr. Qing Zhao, and Sanjuna Stalin for helpful and inspiring discussions.

Conflict of Interest

The authors declare no conflict of interest.

Keywords

dendritic electrodeposition, energy storage, hybrid anodes, sodium metal batteries

Received: May 21, 2019

Revised: July 24, 2019

Published online: September 4, 2019

- [1] A Levelized Cost and Levelized Avoided Cost of New Generation Resources in the Annual Energy Outlook, U.S. Energy Information Administration, **2019**.
- [2] Y. M. Chiang, L. Su, M. S. Pan, Z. Li, *Joule* **2017**, 1, 212.
- [3] J. Wang, J. Yang, Y. Nuli, R. Holze, *Electrochem. Commun.* **2007**, 9, 31.
- [4] S. Wei, L. Ma, K. E. Hendrickson, Z. Tu, L. A. Archer, *J. Am. Chem. Soc.* **2015**, 137, 12143.
- [5] S. Wei, S. Xu, A. Agrawal, S. Choudhury, Y. Lu, Z. Tu, L. Ma, L. A. Archer, *Nat. Commun.* **2016**, 7, 11722.
- [6] P. Hartmann, C. L. Bender, M. Vracar, A. K. Dürr, A. Garsuch, J. Janek, P. Adelhelm, *Nat. Mater.* **2013**, 12, 228.
- [7] C. L. Bender, P. Hartmann, M. Vracar, P. Adelhelm, J. Janek, *Adv. Energy Mater.* **2014**, 4, 1301863.
- [8] K. Song, D. A. Agyeman, M. Park, J. Yang, Y.-M. Kang, *Adv. Mater.* **2017**, 29, 1606572.
- [9] X. Lin, Q. Sun, H. Yadegari, X. Yang, Y. Zhao, C. Wang, J. Liang, A. Koo, R. Li, X. Sun, *Adv. Funct. Mater.* **2018**, 28, 1801904.
- [10] Y. Ansari, K. Virwani, S. Yahyazadeh, L. E. Thompson, E. Lofano, A. Fong, R. D. Miller, Y. La, *Adv. Energy Mater.* **2018**, 8, 1802603.
- [11] S. Wu, Y. Qiao, K. Jiang, Y. He, S. Guo, H. Zhou, *Adv. Funct. Mater.* **2018**, 28, 1706374.
- [12] C. Liu, M. Carboni, W. R. Brant, R. Pan, J. Hedman, J. Zhu, *ACS Appl. Mater. Interfaces* **2018**, 10, 135534.
- [13] F. Cai, Z. Hu, S. Chou, *Adv. Sustainable Syst.* **2018**, 2, 1800060.
- [14] Z. W. Seh, J. Sun, Y. Sun, Y. Cui, *ACS Cent. Sci.* **2015**, 1, 449.
- [15] Z. Zheng, X. Zeng, H. Ye, F. Cao, Z. Wang, *ACS Appl. Mater. Interfaces* **2018**, 10, 30417.
- [16] S. Choudhury, S. Wei, Y. Ozhabes, D. Gunceler, M. J. Zachman, Z. Tu, J. H. Shin, P. Nath, A. Agrawal, L. F. Kourkoutis, T. A. Arias, L. A. Archer, *Nat. Commun.* **2017**, 8, 1.
- [17] S. Wei, S. Choudhury, J. Xu, P. Nath, Z. Tu, L. A. Archer, *Adv. Mater.* **2017**, 29, 1605512.
- [18] T. Oshima, M. Kajita, *Int. J. Appl. Ceram. Technol.* **2004**, 1, 269.
- [19] N. Kawakami, Y. Iijima, in *2010 IEEE Int. Symp. Ind. Electron.*, IEEE, Bari, Italy **2010**, p. 2371.
- [20] Y. Yui, M. Hayashi, J. Nakamura, *Sci. Rep.* **2016**, 6, 22406.
- [21] K. N. Wood, E. Kazyak, A. F. Chadwick, K. Chen, J. Zhang, K. Thornton, N. P. Dasgupta, *ACS Cent. Sci.* **2016**, 2, 790.
- [22] M. Foulletier, G. Pascal, *Solid State Ionics* **1988**, 30, 1172.
- [23] D. A. Stevens, J. R. Dahn, *J. Electrochem. Soc.* **2001**, 148, A803.
- [24] K. Nobuhara, H. Nakayama, M. Nose, S. Nakanishi, H. Iba, *J. Power Sources* **2013**, 243, 585.
- [25] J. Sun, C. Guo, Y. Cai, J. Li, X. Sun, W. Shi, S. Ai, C. Chen, F. Jiang, *Electrochim. Acta* **2019**, 309, 18.